American Mineralogist, Volume 79, pages 51–62, 1994

Determination of accurate $^{[4]}Fe^{3+}$, $^{[6]}Fe^{3+}$, and $^{[6]}Fe^{2+}$ site populations in synthetic annite by Mössbauer spectroscopy

D. G. Rancourt, I.A.D. Christie, M. Royer
Department of Physics, University of Ottawa, Ottawa, Ontario K1N 6N5, Canada

H. Kodama
Centre for Land and Biological Resources Research, Research Branch, Agriculture Canada, Central Experimental Farm, Ottawa, Ontario K1A 0C6, Canada

J.-L. Robert
Centre de Recherches sur la Synthèse et Chimie des Minéraux, CNRS, F-45071 Orléans Cédex 2, France

A. E. Lalonde
Ottawa-Carleton Geoscience Centre, Department of Geology, University of Ottawa, Ottawa, Ontario K1N 6N5, Canada

E. Murad
Bayerisches Geologisches Landesamt, Concordiastraße 28, D-96049 Bamberg, Germany

Abstract

We report accurate $^{[4]}Fe^{3+}$, $^{[6]}Fe^{3+}$, and $^{[6]}Fe^{2+}$ site populations in synthetic annite. They are achieved by detailed analysis of high-quality Mössbauer spectra collected at room temperature, liquid N_2 temperature, and liquid He temperature. The experimental difficulties related to (1) site-specific recoilless fractions, (2) absorber thickness and polarization effects, and (3) absorber texture effects are rigorously addressed. A new quadrupole splitting distribution method that allows arbitrary shape distributions for each site is used for the spectral analysis. It resolves the three sites in accordance with visible spectral features and reveals a needed defect $^{[6]}Fe^{2+}$ site.

Whereas subspectral areas are generally believed to have optimal accuracies of a few percent of total spectral areas, we obtain site population to $\pm 0.2\%$ for Ni + NiO buffered synthetic annite: $^{[4]}Fe^{3+}/Fe = 4.00 \pm 0.15\%$, $^{[6]}Fe^{3+}/Fe = 7.00 \pm 0.20\%$, and $^{[6]}Fe^{2+}/Fe = 89.00 \pm 0.20\%$. These populations suggest that 16.5% of the H in the ideal structural formula, $KFe_3AlSi_3O_{10}(OH)_2$, is missing because of charge-balance requirements: $^{[6]}Fe^{2+} + OH^- \rightleftharpoons {}^{[6]}Fe^{3+} + O^{2-} + H\uparrow$ where $^{[6]}Fe^{3+} + {}^{[4]}Al^{3+} \rightleftharpoons {}^{[4]}Fe^{3+} + {}^{[6]}Al^{3+}$ also occurs.

Introduction

Several recent advances in the methodology of Mössbauer spectroscopy have a direct bearing on the accuracy with which site populations can be determined in Fe-bearing minerals. These include (1) thickness effect evaluations for absorbers with intrinsically broad lines (Ping and Rancourt, 1992; Rancourt et al., 1993), (2) ideal absorber thickness determinations (Long et al., 1983; Rancourt et al., 1993), (3) analytic methods for removing the spectral distortions of the thickness effect (Rancourt, 1989), (4) Voigt-based spectral line shapes for absorbers with quadrupole splitting distributions (QSD) (Rancourt and Ping, 1991; Ping et al., 1991), (5) criteria for identifying distinct spectral contributions (Rancourt et al., 1992; Rancourt, 1993), and (6) methods for determining site-specific recoilless fractions (Royer, 1991). Here, we report the first application of these methods in an attempt to obtain the best possible accuracy of site populations in an Fe-bearing mineral. We demonstrate that an accuracy of 0.2% of Fe_{tot} is possible, whereas the generally accepted limit is 2–5% of Fe_{tot}.

We choose annite because of the predominant role of Fe in its overall crystal chemistry, with $^{[4]}Fe^{3+}$, $^{[6]}Fe^{3+}$, and $^{[6]}Fe^{2+}$ populations being controlled by both structural constraints and thermodynamic conditions (Hazen and Wones, 1972). Better site populations here give an improved evaluation of early annite crystal-chemistry models.

In applying the above methods to annite, we illustrate one of the major difficulties in obtaining site populations using Mössbauer spectroscopy: a given fitting model applied to a given spectrum does not, in general, produce unique populations. This is an intrinsic limitation of non-linear least-squares minimization problems that is often not recognized by spectroscopists. Instead of a unique solution, one obtains a domain of possible values in the space of the resolved site populations. Spectra collected at different temperatures give rise to solution domains that may have relatively small intersections, thereby significantly constraining the possible site populations.

We have obtained four solution domains from (1) model fits to the room-temperature (RT) spectrum, (2) model

0003–004X/94/0102–0051$02.00

fits to the liquid N_2 temperature (LNT) spectrum, (3) analysis independent of line-shape model of the RT dimensionless, intrinsic-absorber, resonant cross section, and (4) analysis independent of line-shape model of the liquid He temperature (LHeT) spectrum. Since the Fe_{tot} is known, combining any two of the above solution domains gives unique $^{[4]}Fe^{3+}$, $^{[6]}Fe^{3+}$, and $^{[6]}Fe^{2+}$ populations, with different associated errors. In this sense, the site populations have been obtained by several independent methods. In particular, we stress that the LHeT evaluation is a truly independent measurement because annite is magnetically ordered at LHeT (Christie et al., 1991), and the hyperfine structure of the spectrum collected at this temperature is magnetically resolved.

The structural formula unit for ideal annite (including formal charges and 2:1 layer cation coordinations) is

$$K^{+}{}^{[6]}Fe_3^{2+}{}^{[4]}Al^{3+}{}^{[4]}Si_3^{4+}O_{10}^{2-}(OH)_2^{-}. \quad (1)$$

Although the ideal analogue end-members in which $^{[6]}Fe^{2+}$ is replaced by $^{[6]}Ni^{2+}$,$^{[6]}Mg^{2+}$ (phlogopite end-member), $^{[6]}Cu^{2+}$ or $^{[6]}Co^{2+}$ are believed to occur, Hazen and Wones (1972) argued that the ideal annite end-member does not occur because of structural constraints involving the mismatch of tetrahedral and octahedral sheets.

They argued that in annite this mismatch is primarily alleviated by the oxyannite reaction

$$^{[6]}Fe^{2+} + OH^{-} \rightarrow {}^{[6]}Fe^{3+} + O^{2-} + H\uparrow \quad (2)$$

which replaces relatively large $^{[6]}Fe^{2+}$ cations by $^{[6]}Fe^{3+}$. They stated that this theory was supported by a subsequent study employing Mössbauer spectroscopy (Wones et al., 1971) and that the latter study "confirmed that at least 10 mole percent of octahedral iron in all synthetic annites is in the trivalent state." Our synthetic annite contains 7.3 mol% of $^{[6]}Fe$ in the trivalent state.

An earlier Mössbauer study (Häggström et al., 1969) had already observed a large amount of Fe^{3+} in a synthetic annite sample, and the only other Mössbauer study of synthetic annite (Ferrow, 1987a, 1987b) also clearly observes Fe^{3+} (both $^{[6]}Fe^{3+}$ and $^{[4]}Fe^{3+}$) in a room-temperature spectrum. The presence of $^{[4]}Fe^{3+}$ was not explained in the latter study, and accurate site populations were not attempted. Dyar and Burns (1986) studied three annite samples, with the most Fe-rich of these having 84% of the amount of Fe contained in a synthetic annite sample. They reported $^{[4]}Fe^{3+}/Fe = 0–10\%$ and $Fe^{3+}/Fe = 11–55\%$.

If a tetrahedral-octahedral mismatch is a major factor controlling site populations in annite, then the Fe^{3+}/Al^{3+} exchange

$$^{[6]}Fe^{3+} + {}^{[4]}Al^{3+} \rightarrow {}^{[6]}Al^{3+} + {}^{[4]}Fe^{3+} \quad (3)$$

is a more effective mechanism for reducing the relatively large lateral extension of the $^{[6]}Fe^{2+}$ sheet than the oxyannite reaction alone. That suggests that once the structural constraints are satisfied, the relative amounts of $^{[4]}Fe^{3+}$ and $^{[6]}Fe^{3+}$ depend on the reducing ability of the environment at synthesis. The essential step in testing these and other ideas concerning the cause of site populations in annite is to obtain accurate $^{[4]}Fe^{3+}$ and $^{[6]}Fe^{3+}$ populations.

Sample synthesis and characterization

The synthesis was performed by J.-L. Robert at Orléans and was achieved in the following way.

The starting material was a fine mechanical mixture of a specially prepared silicate gel and metallic Fe powder. Such a mixture allows fast and reproducible equilibration under the experimental conditions used (Julliot et al., 1987).

The gel contained half of the Fe_{tot} and was prepared by the method of Hamilton and Henderson (1968) using the following reagents: high-grade K_2CO_3 transformed into KNO_3 by reaction with HNO_3, a titrated nitrate solution of Al, a titrated nitrate solution of Fe, and tetraethylorthosilicate (T.E.O.S.), for silica.

The starting mixture and 20 wt% of distilled H_2O were sealed into a Pt tube by arc welding. The synthesis was performed at 600 ± 5 °C and P_{H_2O} of 2.00 ± 0.05 kbar, in a cold-seal Tuttle-type externally heated pressure vessel, with an experiment duration of 3 weeks.

The f_{O_2} was controlled by the Ni + NiO buffer, using the double capsule (Au,Pt) method devised by Eugster (1957). Under our experimental conditions, this buffer sets an f_{O_2} of $10^{-19.1}$ bars (Huebner and Sato, 1970). This f_{O_2} is approximately that set by the alloy constituting the pressure vessel.

Powder X-ray diffraction (XRD) indicated that the experiment product was entirely a single phase of mica. The data were consistent with the 1M polytype structure having unit-cell parameters of $a = 5.393(2)$, $b = 9.342(1)$, $c = 10.332(3)$ Å, $\beta = 100.1(2)°$, and $V = 512.5$ Å^3. These are similar to those given by Hazen and Burnham (1973) for annite from Pikes Peak ($a = 5.3860$, $b = 9.3241$, $c = 10.2683$ Å, $\beta = 100.63°$, and $V = 506.8$ Å^3).

Fe-bearing impurities were not detected in any of the Mössbauer spectra or in any of the Squid (superconducting quantum interference device) magnetometry measurements performed between 4.2 and ~250 K. In addition, no signs of impurities were seen in any of the scanning electron microscope (SEM) pictures. These show that the synthetic annite is very fine grained, with the largest crystals having typical dimensions of 1–2 μm and the smallest crystals being typically ~0.1 μm (Fig. 1).

Several low-field Squid magnetometry measurements (0.5–30 G) revealed a magnetic ordering temperature at $T_c = 58 \pm 1$ K. This is the highest ordering temperature ever observed in any layer silicate and possibly in any magnetically two-dimensional material. It is indicative of a large Fe^{2+} loading of the octahedral sheets.

The Squid data on the 30 G susceptibility of the powder follow the Curie-Weiss law at $T \gtrsim 60$ K. Analysis of these data in the range of 100–150 K yields a Curie-Weiss temperature $\theta_{CW} = 60 \pm 2$ K and a Curie constant C = 0.020 ± 0.002 emu·K/g. The predicted value of C for

ideal annite ($^{[6]}Fe^{2+}/Fe = 100\%$) having the cell volume $V = 512.5$ Å^3 and corresponding ideal density $\rho = 3.317$ g/cm^3 is (6/V) $(p_{eff}\mu_B)^2/3k_B\rho = 0.021$ emu·K/g, where μ_B is the Bohr magneton, k_B is the Boltzmann constant, and $p_{eff} = 5.4$ is the effective Bohr magneton number for an Fe^{2+} ion (Ashcroft and Mermin, 1976). Letting 11% of the Fe be Fe^{3+} implies a $p_{eff} \simeq 5.46$ and gives a predicted C = 0.022 emu·K/g. The Squid magnetometry results therefore give an upper limit for Fe^{3+}/Fe of ~10%.

Infrared absorption in the OH-ion stretching mode region showed the expected dominant N band at 3665 cm^{-1}, with a full width at half maximum of 30 cm^{-1}. The N band arises from OH ions for which the three immediately neighboring octahedral sites are filled with divalent ions (Vedder, 1964), here Fe^{2+}-Fe^{2+}-Fe^{2+}. In addition, two small bands of comparable intensity having widths of ~30 cm^{-1} are present at 3580 and 3545 cm^{-1}. We interpret these as I bands, which are caused by OH ions having one of the three closest octahedral sites occupied by a trivalent ion (Vedder, 1964), and refer to them as I_a and I_b, respectively. This assignment is supported by the fact that I_b grows dramatically (remaining at 3545 cm^{-1}) and becomes comparable in intensity to the N band when the annite sample is oxidized by heating in air (Christie et al., 1993). We therefore attribute I_a and I_b to Fe^{2+}-Fe^{2+}-Al^{3+} and Fe^{2+}-Fe^{2+}-Fe^{3+} configurations, respectively. Their relative intensities are consistent with the amounts of $^{[6]}Al^{3+}$ and $^{[6]}Fe^{3+}$ obtained by Mössbauer spectroscopy in the present study. When V bands (caused by OH ions close to octahedral vacancies) are present, they occur at lower frequencies than I bands (Vedder, 1964). No other distinct bands are present down to 3000 cm^{-1} that might be attributed to V bands. Thus, the infrared absorption spectrum indicates the presence of $^{[6]}Al^{3+}$ and $^{[6]}Fe^{3+}$ and the relative absence of octahedral vacancies.

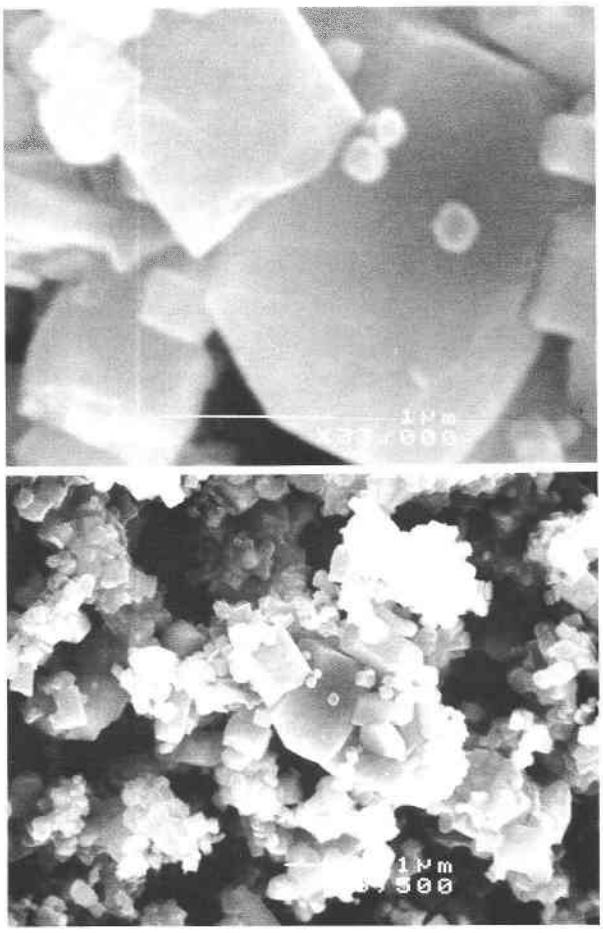

Fig. 1. Scanning electron microscope pictures of the synthetic annite at high **(top)** and low **(bottom)** magnifications. The thin white horizontal bars represent 1 µm.

Experimental methods and analysis

Collection and calibration

Transmission ^{57}Fe Mössbauer spectra were obtained, calibrated, and folded in the usual way (e.g., Rancourt et al., 1992). Folding is essential to produce flat backgrounds with parameters that do not trade off with those of the absorption patterns when least-squares fitting is performed.

The RT center shifts (with RT = 22 °C) are referenced to metallic Fe at RT; however, the center shifts at LNT and LHeT depend on the ^{57}Fe center shifts of the ^{57}Co-Rh source at LNT and LHeT, respectively, and are therefore not known accurately.

All the spectra except one were collected at Ottawa. Two LHeT spectra were collected: one at $T = 7.0$ K was collected at Ottawa, and one at $T = 4.2$ K was collected at Technische Universität München by Murad. The München data were collected in the sine mode rather than in the constant acceleration mode of the transducer. No significant difference can be seen between these two LHeT spectra, and both were analyzed for the present study.

The low-temperature experiments were done in a He exchange gas cryostat, with the source and absorber at the same temperature, although the source temperature was not measured directly.

The cryogenic absorber was prepared as follows and was also used at RT in the cryostat. A Cu holder with ultra-pure Al windows 1.40 cm in diameter was uniformly loaded with 81.5 mg of the annite powder. The powder was hand pressed between the two Al windows to ensure mechanical stability and thermal contact. The holder is not gas-tight and allows exchange gas to penetrate.

Rancourt (1989) recently described all of the factors that need to be considered when accurate site populations from Mössbauer spectroscopy are required. We next address each of these that are relevant to the present case.

Spectrum quality: Signal to noise ratio

Fitting models must rely on distinct observed spectral features. Therefore, the best possible statistics should be

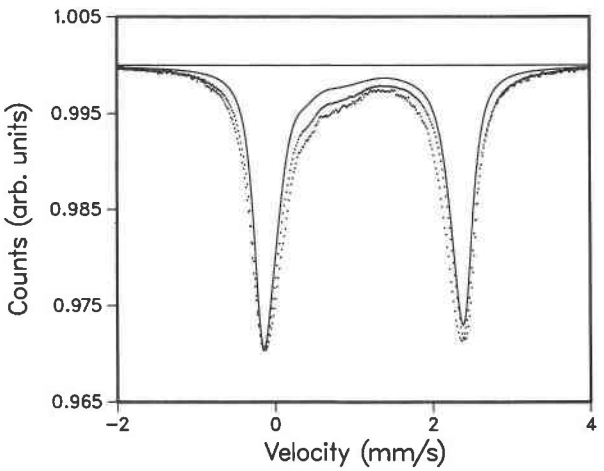

Fig. 2. Two experimental spectra (dots) and one calculated spectrum (solid line) are scaled to the same signal depth and compared. They are also taken to have the same arbitrary BG level of 1.0 (solid horizontal line). The spectrum with the broadest lines corresponds to the 90-mg/cm² absorber. The other experimental spectrum corresponds to the 53-mg/cm², nearly ideal thickness absorber. The calculated spectrum is a simulation based on the extracted dimensionless, intrinsic-absorber, resonant cross section [using $\sigma_a(E) = \sigma'_a(E)/f\,n_a$ in Eq. 2 of Ping and Rancourt, 1992] and shows the spectrum that would be measured in the thin absorber limit if this limit could be attained.

obtained. To achieve this we use the ideal absorber thickness for annite. This thickness gives the largest signal to noise (S/N) ratio in a given accumulation time and is ~50 mg/cm² for annite (Rancourt et al., 1993; Long et al., 1983). R*T* spectra were also collected at 35, 61, and 90 mg/cm² to gauge the impact of thickness effects on fitted spectral areas.

Absorber thickness effects

At a given absorber thickness, thickness effects are particularly severe for spectra containing small numbers of intrinsically thin absorption lines but are much less significant when the absorption is divided into many and intrinsically broad lines. New methods for calculating the expected thickness attenuation of intrinsically broad lines have recently been developed (Rancourt et al., 1993; Ping and Rancourt, 1992). These suggest that, for annite, significant thickness attenuation should occur at the thicknesses we have used. This implies that a full thickness correction procedure (Rancourt, 1989) should be applied to yield the intrinsic absorber cross section.

We have applied this procedure to our 53-mg/cm² R*T* spectrum and have analyzed the extracted intrinsic absorber cross section. We find that the site-specific relative subspectral areas are the same within uncertainties as those obtained from fitting the raw 53-mg/cm² spectral data. It seems therefore that, in this case, the non-negligible thickness-related spectral distortions and main peak attenuations do not significantly affect the extracted subspectral relative areas with the fitting model line shapes that we have used. This is true despite the noticeable thickness distortions that are shown to increase systematically with thickness in Figure 2. The simulated spectrum for the thin-sample limit is also shown for comparison. Representative extracted Fe^{3+}/Fe values are 11.0–11.2% at 0–53 mg/cm², ~11.5% at 61 mg/cm², and ~11.7% at 90 mg/cm².

That we are effectively in the thin limit for those quantities that interest us is supported by the additional facts that (1) the LN*T* spectrum (53 mg/cm² absorber) is thicker because of larger recoilless fractions and has a different line shape because of larger quadrupole splittings (QS), yet it gives the same relative subspectral areas as the R*T* spectra; and (2) the LHe*T* hyperfine spectra are magnetically split and consist of very broad lines from hyperfine field distributions coupled with quadrupole splitting distributions, yet they also give the same subspectral areas. The latter point is significant because such a hyperfine structure should dramatically reduce the effective absorber thickness.

Polarization effects

Polarization effects can occur in addition to ordinary thickness effects when the Mössbauer radiation is polarized, as it is resonantly absorbed on traversing the finite thickness absorber. This, in general, can occur in single-crystal or textured absorbers but will not occur in sufficiently fine and nontextured absorbers (see section on absorber texture below).

For a given amount per squared centimeter of a polarizing material or mineral, a textured or single-crystal sample gives rise to greater spectral distortions than a nontextured fine powder absorber of the same material. For this reason, an absorber that is expected to be thin on the basis of calculations of the effect of ordinary thickness (e.g., Ping and Rancourt, 1992) may, in fact, be thick if it contains polarizing material.

These considerations are important to the present application because (1) all materials that give rise to quadrupole doublets are Mössbauer polarizing materials, and (2) no general and practical procedure presently exists to correct for polarization effects arising from real absorbers with intrinsically broad absorption lines, such as those found in all Fe-bearing silicate minerals.

Fortunately, our annite is a very fine powder (a clay in fact, see Fig. 1) and our absorbers are nontextured (next section) such that polarization effects are negligible in this application. This is supported by the fact that exact ordinary absorption corrections of the R*T* spectrum gave consistent results (previous section).

Absorber texture

A nontextured absorber is a powder or polycrystalline sample in which all of the crystal orientations are represented with equal probabilities. If there is a preferred orientation, then the absorber is textured.

If the Goldanskii-Karyagin effect and dynamic line shape effects are barred, nontextured absorbers have

spectra composed of elemental quadrupole doublets that have equal intensities of their high- and low-energy Lorentzian line components. This supplies welcome constraints for the fitting models that are applied to the spectral data. In this study, these constraints were essential.

Texture is particularly difficult to avoid in layer silicates where the cleavage gives rise to flakes that prefer the plane of the absorber. However, with the claylike nature of our annite (Fig. 1), using a relatively thick absorber (of near ideal thickness 53 mg/cm^2) gave a complete absence of texture.

We checked this by rotating our 53-mg/cm^2 absorber by 30 and 54°, which gave thicknesses of 61 and 90 mg/cm^2, respectively. All of the spectral changes (Fig. 2) can be attributed to thickness effects alone, with no change in intrinsic doublet symmetries. Furthermore, our fitting models that assume complete absence of texture gave statistically ideal and physical fits and no evidence of systematic differences that could be attributed to a small amount of texture.

The 35-mg/cm^2 absorber also showed a total absence of texture; however, a 6.2-mg/cm^2 absorber showed obvious signs of texture. Using the near ideal thickness of 53 mg/cm^2 therefore has the double advantage of giving good spectrum quality and ensuring that, with this claylike sample, there is no texture. Having to account for thickness effects is a worthwhile compromise in view of these advantages.

Quadrupole splitting distributions (QSD)

In modeling the spectra, it is advantageous to use as many physical constraints as can be rigorously justified. Here, the choice of the model line shape is the first consideration. Although elemental lines that are due to single groups of identical probe environments must, in the absence of thickness effects and other artifacts, be Lorentzian lines, absorption lines that are made up of several overlapping Lorentzians are not Lorentzian in shape.

A given species in a given anion coordination, $^{[6]}Fe^{2+}$ say, has many different local environments that are defined by local distortions, local charge distributions, the types and positions of nearest neighbor anions, next nearest neighbor cations, etc. Each local environment gives rise to a single elemental quadrupole doublet such that a continuous distribution of quadrupole splittings can be used to model the overall absorption doublet.

A powerful new method for fitting with distributions has been developed (Rancourt and Ping, 1991) and has been applied to quadrupole splittings recently (Ping et al., 1991). We use this method here and therefore briefly describe it.

Each local environment has its own quadrupole splitting (Δ) and also has its own center shift (δ). Since, for a given species and anion coordination, Δ depends much more strongly on the local environment than does δ, we assume that δ and Δ are linearly coupled:

$$\delta = \delta_0 + \delta_1 \cdot \Delta \tag{4}$$

and distribute only Δ. That is, by optimization we obtain a distribution, $P(\Delta)$, of quadrupole splittings that automatically has an associated distribution of δ through Equation 4.

The coupling parameters δ_0 and δ_1 are characteristic of a particular group of probe ions (e.g., of a particular species or of a particular species and anion coordination, etc.). Rancourt and Ping (1991) referred to such a group, one that has its own $P(\Delta)$ and its own values of δ_0 and δ_1, as a site. In the present applications to annite at RT and LNT (above the magnetic ordering temperature), it turns out that only three such sites with independent Δ distributions are required and that these correspond to $^{[4]}Fe^{3+}$, $^{[6]}Fe^{3+}$, and $^{[6]}Fe^{2+}$, that is, only the valence state and coordination number give rise to distinct spectral components. All other information concerning more subtle structural features [e.g., cis and trans octahedral sites, FeO_6^{2-} and $FeO_5^{2-}OH^-$ coordinations rather than $FeO_4^{2-}(OH^-)_2$ at octahedral sites, etc.] is taken into account by the Δ distributions. Rancourt (unpublished manuscript) has established that quantitative populations for cis and trans $^{[6]}Fe^{2+}$ sites cannot be obtained by Mössbauer spectroscopy in trioctahedral micas. The cis and trans sites are not resolved but only contribute to the overall QSD, $P(\Delta)$.

We assume that a true $P(\Delta)$ can be expressed as a sum of Gaussian components:

$$P(\Delta) = \sum_{i=1}^{N} p_i G_i(\Delta_{0i}, \sigma_{\Delta i}; \Delta) \tag{5}$$

where the p_i is a weight factor such that $\Sigma p_i = 1$ and each Gaussian, G_i, is normalized to an area of 1. Each Gaussian has a center position, Δ_{0i}, and a Gaussian half-width, $\sigma_{\Delta i}$. Only as many Gaussians, N, as are required by the data are used: most often $N = 1$ or $N = 2$ is sufficient. This is because the Gaussians are intrinsically suitable for describing real distributions.

The power of the technique lies in that the corresponding line shape, $Q(v)$, for a given site can be shown analytically to be a sum of Voigts (Rancourt and Ping, 1991):

$$Q(v) = \sum_{i=1}^{N} p_i \sum_{k=\pm 1} V_{ik}(\delta_0 + \delta_1\Delta_{0i} + k\Delta_{0i}/2, \; |\delta_1 + \tfrac{1}{2}|\sigma_{\Delta i}, \gamma, h_k; v) \tag{6}$$

where γ is the underlying Lorentzian full width at half maximum (FWHM) and h_k is the underlying Lorentzian height. For nontextured thin absorbers we should have $h_+ = h_-$ (symmetric elemental doublets) and $\gamma = 0.194$ mm/s (Heisenberg value for ^{57}Fe).

Using this line shape $Q(v)$ in a configuration of one site and one component ($N = 1$) with $h_+ = h_-$ and $\gamma = 0.194$ mm/s requires six free parameters: h, δ_0, δ_1, Δ_0, σ_Δ, and a flat background level, BG. By comparison, two equal-area Lorentzian lines that are allowed to have different widths [the two Voigt lines in the $N = 1$ $Q(v)$ have different widths through δ_1] also require six free parameters: two centers, two γ's, one area, and a BG.

TABLE 1. R*T* spectrum fit parameters

Fit	γ	BG	A_{tot}	$\delta_0\langle 3+\rangle$	$\delta_0[3+]$	$\delta_0[2+]$	$\delta_1[2+]$	$\Delta_0\langle 3+\rangle$	$\sigma_\Delta\langle 3+\rangle$	$\Delta_0[3+]$	$\sigma_\Delta[3+]$
1-1-2	0.2798	720.33	269.65	0.2523	0.4363	1.2322	−0.0459	0.5440	0.0076	0.9682	0.5484
1-1-3a	0.2843	720.71	273.00	0.1641	0.4185	1.2250	−0.0422	0.5438	0.0001	0.9135	0.5498
1-1-3b	0.2844	720.70	272.89	0.1667	0.4227	1.2273	−0.0431	0.5397	0.0001	0.9207	0.5367
1-1-3c	0.2848	720.69	272.87	0.1687	0.4256	1.2316	−0.0449	0.5365	0.0001	0.9293	0.5206
1-1-3d	0.2853	720.69	272.85	0.1712	0.4273	1.2368	−0.0470	0.5327	0.0001	0.9381	0.5026
1-1-3e	0.2856	720.69	272.89	0.1706	0.4262	1.2416	−0.0489	0.5347	0.0001	0.9468	0.4921
1-1-3f	0.2856	720.69	272.86	0.1721	0.4275	1.2421	−0.0491	0.5327	0.0001	0.9475	0.4843
1-1-3g	0.2858	720.69	272.89	0.1732	0.4281	1.2436	−0.0497	0.5311	0.0001	0.9493	0.4754
1-1-3h	0.2859	720.69	272.85	0.1741	0.4281	1.2455	−0.0505	0.5302	0.0001	0.9517	0.4657
1-1-3i	0.2861	720.68	272.85	0.1765	0.4284	1.2485	−0.0518	0.5279	0.0001	0.9519	0.4443
1-1-3j	0.2865	720.69	272.89	0.1748	0.4173	1.2618	−0.0569	0.5315	0.0001	0.9815	0.4203
1-1-3k	0.2862	720.69	272.86	0.1770	0.4138	1.2650	−0.0582	0.5296	0.0001	0.9806	0.3950
1-1-3l	0.2817	720.69	272.71	0.1762	0.4048	1.2734	−0.0615	0.5317	0.0001	0.9840	0.3610

Note: symmetric elemental doublets are assumed ($h_+ = h_-$) for all sites. Parameters γ, δ_0, Δ_0, and σ_Δ are in millimeters per second. The $\langle 3+\rangle$, [3+], and [2+] refer, respectively, to $^{[4]}Fe^{3+}$-, $^{[6]}Fe^{3+}$-, and $^{[6]}Fe^{2+}$-specific parameters. BG is in kilocounts. The total absorption area

$$A_{tot} \equiv \pi/2\,\gamma \sum_{\text{sites}}^{3} \sum_{i}^{N} \sum_{k=\pm 1} p_i h_k$$

(Eq. 6) is in kilocounts times millimeters per second. Parameter δ_1 (Eq. 4) is dimensionless. The site- and component-specific areas ($a\langle 3+\rangle$, etc.) are in percentages of A_{tot}. Except in the 1-1-2 fit, $a\langle 3+\rangle$ and $\sigma_\Delta\langle 3+\rangle$ are frozen parameters that are not adjusted in the fitting process.

The Qv line shapes in a one-site, N-component configuration with $h_+ = h_-$ and free γ require $4 + 3N$ free parameters. Our final fits to R*T* and LN*T* spectra require three sites attributable to $^{[4]}Fe^{3+}$, $^{[6]}Fe^{3+}$, and $^{[6]}Fe^{2+}$. Each site gives distinct, characteristic, visible features in the spectra (e.g., Rancourt et al., 1992). Both $^{[4]}Fe^{3+}$ and $^{[6]}Fe^{3+}$ require only $N = 1$; however, the $^{[6]}Fe^{2+}$ site requires $N = 3$. The resulting model is referred to as a 1-1-3 model. For the Fe^{3+} sites, we always set $\delta_1 = 0$, and the γ is always common to all sites. This gives a maximum of 21 free parameters in our 1-1-3 model fits.

Parameter tradeoffs

As mentioned above, even for a given fitting model that uses physically correct line shapes and that introduces only as many free parameters as are required to obtain statistically acceptable fits, a fundamental problem persists: the solution obtained by minimization is usually not unique. Entire regions in the parameter space give equally good and acceptable fits. This problem is particularly severe in cases like the present one, where considerable line overlap occurs.

Since we are mainly concerned with subspectral (i.e., site-specific) areas to obtain site populations, we examine how these areas trade off with each other. We find that the Mössbauer solution, for, say, 1-1-3 fits to the R*T* spectrum, corresponds to an entire line segment of finite length in the three dimensional space of the populations $^{[4]}Fe^{3+}$, $^{[6]}Fe^{3+}$, and $^{[6]}Fe^{2+}$.

All the points on this line segment give equally good 1-1-3 fits at R*T* by changing (i.e., trading off) the values of several of the fitting parameters that are dependent on each other through the spectrum shape. Such a solution domain (Rancourt et al., 1985) of equivalent Mössbauer solutions can always be mapped out completely by imposing fixed values on some of the dependent parameters.

The LN*T* spectrum yields its own solution domain. If the latter intersects the R*T* domain, then the Mössbauer solution can be significantly reduced, in our case to a single point in the population space. A third measurement, such as a very different LHe*T* spectrum, can further reduce the solution or, in our case, corroborate the already unique solution.

That is the main idea. Once a line shape model has been carefully chosen based on physical and statistical considerations, we identify the solution domains and attempt to reduce the Mössbauer solution by using several measurements.

Recoilless fractions

In the absence of thickness and polarization effects, the subspectral area, A_i, for site i is related to the corresponding site population as

$$A_i = \pi/2\ \eta_M f_s \sigma_0 \Gamma_0 f_{ai} n_{ai} \tag{7}$$

where η_M is the part of the BG level that corresponds to Mössbauer (14.4 keV) γ-rays, f_s is the recoilless fraction of the source, σ_0 is the cross section at resonance for the Mössbauer transition, Γ_0 is the natural FWHM of the Mössbauer transition ($\Gamma_0 = 0.097$ mm/s), f_{ai} is the site-specific recoilless fraction of the absorber, and n_{ai} is the number of ^{57}Fe nuclei in site i per unit area of the uniform thickness absorber.

The total spectral area is then a sum over all sites

$$A_{tot} = \sum_j A_j$$

such that the relative site populations are given by

$$\frac{Fe_i}{Fe} = \frac{n_{ai}}{n_a} = \frac{\bar{f}}{f_{ai}} \cdot \frac{A_i}{A_{tot}} \tag{8}$$

where

$$n_a = \sum_j n_{aj}$$

TABLE 1.—*Continued*

Fit	Δ_{01}[2+]	$\sigma_{\Delta 1}$[2+]	Δ_{02}[2+]	$\sigma_{\Delta 2}$[2+]	Δ_{03}[2+]	$\sigma_{\Delta 3}$[2+]	$a\langle 3+\rangle$	a[3+]	a_1[2+]	a_2[2+]	a_3[2+]	χ^2_{red}
1-1-2	2.5527	0.1025	2.2352	0.2812	—	—	3.22	9.65	54.17	32.96	—	3.35
1-1-3a	2.5924	0.0689	2.3224	0.1730	1.6785	0.4364	1.64	10.26	43.05	38.72	6.33	1.12
1-1-3b	2.5919	0.0695	2.3208	0.1756	1.6685	0.4608	1.96	9.85	43.15	38.70	6.33	1.08
1-1-3c	2.5912	0.0702	2.3177	0.1778	1.6504	0.4826	2.30	9.44	43.49	38.49	6.29	1.06
1-1-3d	2.5889	0.0726	2.3080	0.1773	1.6272	0.5040	2.63	9.01	44.97	37.16	6.22	1.05
1-1-3e	2.5896	0.0712	2.3108	0.1794	1.6192	0.5129	2.79	8.81	44.35	37.80	6.25	1.04
1-1-3f	2.5895	0.0714	2.3105	0.1812	1.6125	0.5318	2.96	8.59	44.30	37.88	6.28	1.04
1-1-3g	2.5894	0.0713	2.3103	0.1832	1.5964	0.5463	3.13	8.36	44.24	38.04	6.23	1.04
1-1-3h	2.5892	0.0713	2.3100	0.1849	1.5839	0.5622	3.29	8.13	44.20	38.15	6.23	1.04
1-1-3i	2.5889	0.0714	2.3091	0.1881	1.5675	0.6050	3.62	7.66	44.18	38.22	6.32	1.05
1-1-3j	2.5888	0.0704	2.3061	0.1893	1.5369	0.6165	3.96	7.28	44.09	38.37	6.31	1.05
1-1-3k	2.5886	0.0706	2.3047	0.1922	1.5365	0.6789	4.28	6.81	44.01	38.34	6.56	1.08
1-1-3l	2.5891	0.0730	2.3019	0.1938	1.6869	0.8173	4.54	6.45	43.14	37.71	8.16	1.10

and the average recoilless fraction is given by

$$\bar{f} \equiv \frac{1}{n_a} \sum_j n_{aj} f_{aj}. \quad (9)$$

Equation 8 shows that even relative site populations can only be obtained from spectral areas if site-specific absorber recoilless fractions are known. These recoilless fractions depend on local bonding strengths and configurations and must be measured. They also depend on temperature.

Royer (1991) has made an extensive study of site-specific recoilless fractions in Fe-bearing trioctahedral micas and found that, whereas all the biotite samples studied had larger Fe^{3+} recoilless fractions than Fe^{2+} recoilless fractions in varying degrees, the same synthetic annite sample as studied here had recoilless fractions that were equal for all sites, within experimental accuracy. This finding is corroborated by our study, which finds the same Fe^{3+}/Fe^{2+} spectral area ratios at R*T*, LN*T*, and LHe*T*.

RESULTS AND DISCUSSION

R*T* spectrum

The Fe^{2+} spectral contribution has sufficient structure to require at least two Gaussian components in its QSD. The best 1-1-2 fit that resolves the $^{[4]}Fe^{3+}$, $^{[6]}Fe^{3+}$, and $^{[6]}Fe^{2+}$ sites is shown in Figure 3, and the corresponding fit parameters are given in Table 1.

The two Fe^{2+} Gaussian components should not simply be ascribed to cis and trans sites. They are part of one continuous distribution that cannot be unambiguously resolved into cis and trans contributions. Indeed, equivalent fits can be obtained for an entire range of cis-trans population ratios that actually correspond to essentially identical QSD. This topic will be the subject of a future publication.

The difference spectrum (Fig. 3) of the 1-1-2 fit shows significant discrepancies in the region of the visible Fe^{3+} features (0.1–1.1 mm/s) and, most notabiy, at ~1.7 mm/s. The latter discrepancy is also seen in other Fe-bearing trioctahedral micas (e.g., Hargraves et al., 1990) and suggests the existence of a small family of Fe^{2+} sites that have relatively small QS. This, in turn, suggests that a 1-1-3 fitting model is appropriate. If so, it should also remove the other discrepancies.

The discrepancy observed at ~1.7 mm/s (Fig. 3) is real and does not disappear when the spectrum is corrected for thickness (e.g., Hargraves et al., 1990). It is essential that this inconsistency be resolved since, in our annite, it represents a spectral area comparable in magnitude with the Fe^{3+}-specific subspectral areas. A 1-1-2 fit overestimates Fe^{3+}/Fe, especially $^{[6]}Fe^{3+}/Fe$.

The 1-1-3 model is successful in that it eliminates all previous systematic differences, and it yields a statistically ideal reduced chi-squared of $\chi^2_{red} \simeq 1$. This means that the 1-1-3 model may be the correct physical model: it cannot be ruled out on statistical grounds, as in the case of the 1-1-2 model with $\chi^2_{red} \sim 3$. As mentioned above, however, there remains a fundamental problem of nonuniqueness.

A typical 1-1-3 fit is shown in Figure 4, and the fit parameters for several 1-1-3 fits are given in Table 1. The worst 1-1-3 fit considered is shown in Figure 5.

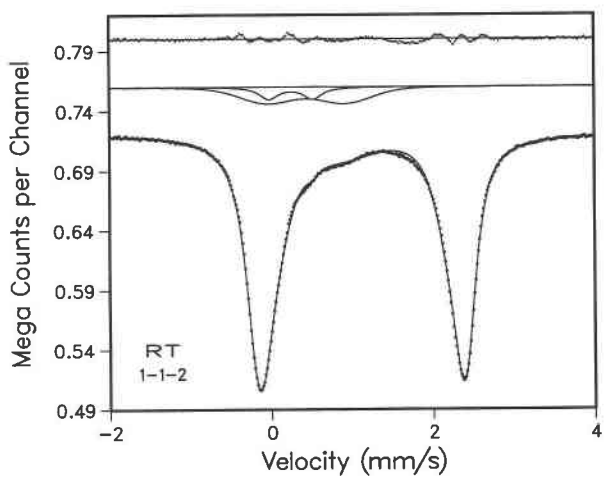

Fig. 3. The solid line running through the spectral data represents the best 1-1-2 fit to the R*T* spectrum that resolves the three Fe sites. The difference spectrum for this fit is shown with the same vertical scale at the top of the figure, where the solid horizontal line indicates the zero-difference level. The subspectral contributions corresponding to $^{[4]}Fe^{3+}$ (narrow doublet) and $^{[6]}Fe^{3+}$ (broad doublet) are shown on a shifted BG level for clarity. The corresponding fit parameters are given in Table 1.

TABLE 2. LN*T* spectrum fit parameters

Fit	γ	BG	A_{tot}	$\delta_0\langle 3+\rangle$	$\delta_0[3+]$	$\delta_0[2+]$	$\delta_1[2+]$	$\Delta_0\langle 3+\rangle$	$\sigma_\Delta\langle 3+\rangle$	$\Delta_0[3+]$	$\sigma_\Delta[3+]$
1-1-2	0.2348	392.72	182.33	0.3823	0.6521	1.2028	+0.0175	0.4739	0.0000	0.6560	0.4052
1-1-3a	0.1990	392.95	183.62	0.3744	0.6015	1.2168	+0.0128	0.4574	0.0001	0.6531	0.4275
1-1-3b	0.2037	392.97	183.86	0.3739	0.6055	1.2131	+0.0140	0.4601	0.0001	0.6553	0.4034
1-1-3c	0.2104	393.00	184.24	0.3734	0.6128	1.2076	+0.0158	0.4655	0.0001	0.6572	0.3646
1-1-3d	0.2157	393.02	184.54	0.3735	0.6217	1.2031	+0.0173	0.4723	0.0001	0.6581	0.3259
1-1-3e	0.2184	393.04	184.75	0.3740	0.6288	1.2008	+0.0181	0.4776	0.0001	0.6582	0.2990

Note: symmetric elemental doublets are assumed ($h_+ = h_-$) for all sites. Parameters γ, δ_0, Δ_0, and σ_Δ are in millimeters per second. The $\langle 3+\rangle$, [3+], and [2+] refer, respectively, to $^{[4]}Fe^{3+}$-, $^{[6]}Fe^{3+}$-, and $^{[6]}Fe^{2+}$-specific parameters. BG is in kilocounts. The total absorption area

$$A_{tot} \equiv \tfrac{\pi}{2}\gamma \sum_{sites}^{3} \sum_{i}^{N} \sum_{k=\pm 1} p_i h_k$$

(Eq. 6) is in kilocounts times millimeters per second. Parameter δ_1 (Eq. 4) is dimensionless. The site- and component-specific areas ($a\langle 3+\rangle$, etc.) are in percentages of A_{tot}. Except in the 1-1-2 fit, $a\langle 3+\rangle$ and $\sigma_\Delta\langle 3+\rangle$ are frozen parameters that are not adjusted in the fitting process.

The 1-1-3 fits differ in the partitioning of the spectral area among the three sites of interest. We illustrate these tradeoff effects by plotting $^{[6]}Fe^{3+}/Fe$ vs. $^{[4]}Fe^{3+}/Fe$ for acceptable 1-1-3 fits of the R*T* spectrum (Fig. 6). This figure also shows the analogous tradeoff curve for 1-1-3 fits of the LN*T* spectrum and the Fe^{3+}_{tot} constraint obtained from both the LHe*T* spectra and the thickness-corrected R*T* spectrum, as explained below.

On both the R*T* and LN*T* trade-off curves shown in Figure 6, the χ^2 remains ideal within approximately 2 sd of its statistically predicted mean value for a correct fitting model.

As we move on these trade-off curves, we also observe some trade-off between the Fe^{3+}_{tot} and the Fe^{2+}_{tot}. For example, on the R*T* curve we go from $Fe^{3+}/Fe = 11.9\%$ at the low $^{[4]}Fe^{3+}$ end to $Fe^{3+}/Fe = 11.0\%$ at the high $^{[4]}Fe^{3+}$ end (Table 1). The LN*T* trade-off curve has a more constrained behavior, with Fe^{3+}/Fe varying between 11.25 and 10.89% (see below).

LN*T* spectrum

Figure 7 shows that, at LN*T* (= 80 K), a 1-1-2 model works better than at R*T* (Fig. 3). The fit (Table 2), however, is again statistically unacceptable ($\chi^2_{red} > 1 + 2\sigma$) and again shows a significant systematic discrepancy on the low-energy side (here at ~2 mm/s) of the high-energy component of the Fe^{2+} absorption. This again suggests the existence of a family of Fe^{2+} local environment sites that have relatively small QS and leads us to 1-1-3 fits. This small QS $^{[6]}Fe^{2+}$ spectral contribution having its own small Gaussian component in the Fe^{2+} QSD and occurring at both R*T* and LN*T* is referred to as the defect Fe^{2+} site or $*Fe^{2+}$ and is discussed further below.

A typical 1-1-3 fit to the LN*T* spectrum is shown in Figure 8, and the fit parameters for all the 1-1-3 fits considered are given in Table 2. The relevant trade-off curve for $^{[6]}Fe^{3+}/Fe$ vs. $^{[4]}Fe^{3+}/Fe$ at LN*T* is plotted in Figure 6, along with the corresponding R*T* curve.

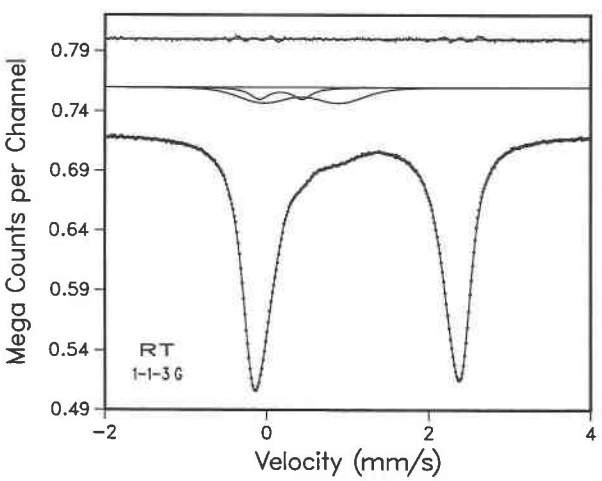

Fig. 4. Typical 1-1-3 fit (1-1-3g fit, Table 1) of the R*T* spectrum of our synthetic annite sample. The display format is the same as in Fig. 3.

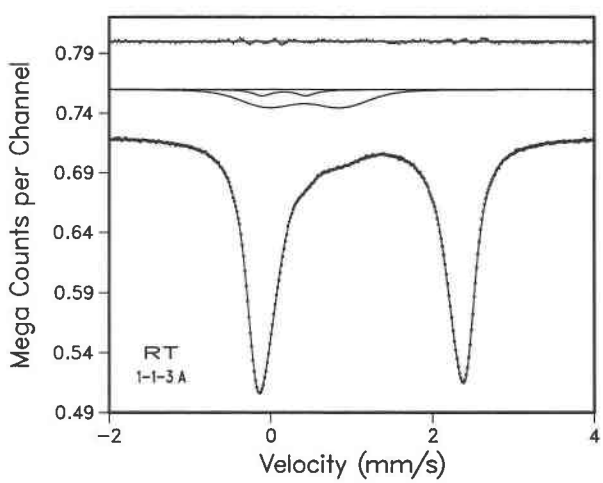

Fig. 5. Worst acceptable fit (1-1-3a fit, Table 1) of the R*T* spectrum. The display format is the same as in Fig. 3.

TABLE 2.—*Continued*

Fit	Δ_{01}[2+]	$\sigma_{\Delta 1}$[2+]	Δ_{02}[2+]	$\sigma_{\Delta 2}$[2+]	Δ_{03}[2+]	$\sigma_{\Delta 3}$[2+]	$a\langle 3+\rangle$	a[3+]	a_1[2+]	a_2[2+]	a_3[2+]	χ^2_{red}
1-1-2	3.0012	0.1273	2.7439	0.2095	—	—	4.00	8.42	57.46	30.12	—	1.34
1-1-3a	3.0027	0.1494	2.7703	0.2415	2.6100	1.3965	2.72	8.53	49.46	31.69	7.59	0.97
1-1-3b	3.0055	0.1451	2.7748	0.2339	2.5355	1.4747	3.13	8.02	48.95	32.74	7.16	0.91
1-1-3c	3.0100	0.1382	2.7830	0.2238	2.3901	1.6245	3.78	7.23	47.73	34.73	6.54	0.87
1-1-3d	3.0142	0.1321	2.7895	0.2156	2.2132	1.8050	4.41	6.48	46.55	36.50	6.05	0.90
1-1-3e	3.0166	0.1287	2.7931	0.2113	2.0664	1.9606	4.83	6.00	45.82	37.52	5.83	0.97

On examining these curves (Fig. 6) and the corresponding data (Tables 1 and 2), we note that the LNT curve gives a relatively narrow range of possible populations compared with the range given by the RT curve alone. This situation arises because the site-specific contributions are better resolved in the LNT spectrum. In particular, the visible $^{[4]}Fe^{3+}$ contribution goes from being a shoulder at RT (0.4 mm/s in Fig. 3) to being a distinct peak at LNT (0.6 mm/s in Fig. 7).

We also note that if these RT and LNT tradeoff curves are plotted (not shown) in the full three-dimensional population space of $^{[6]}Fe^{2+}$ vs. $^{[6]}Fe^{3+}$ and $^{[4]}Fe^{3+}$, then they continue to be represented by line segments, and these line segments come closest to intersecting at their large $^{[4]}Fe^{3+}$ ends, where $Fe^{3+}/Fe \simeq 11.0\%$. This is in contrast to the plot of $^{[6]}Fe^{3+}/Fe$ vs. $^{[4]}Fe^{3+}/Fe$, where the projections of the true tradeoff curves appear as almost parallel line segments.

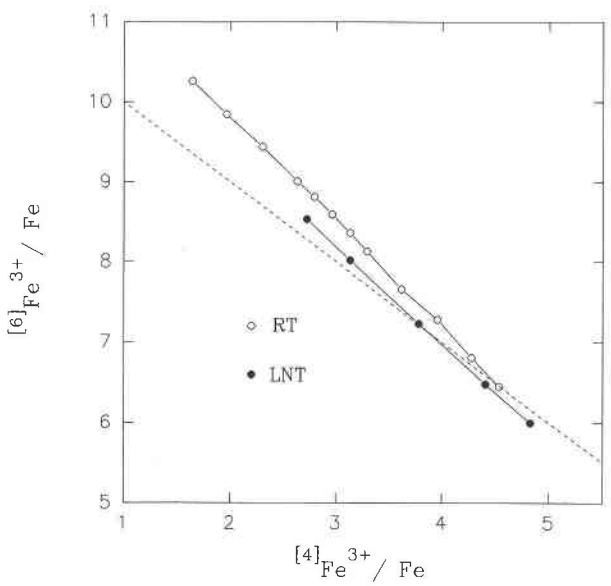

Fig. 6. Plots of $^{[6]}Fe^{3+}/Fe$ vs. $^{[4]}Fe^{3+}/Fe$ (both expressed in percentages) from acceptable 1-1-3 fits for both the RT spectrum (Table 1) and the LNT spectrum (Table 2). The dashed line represents the $Fe^{3+}/Fe = 11.0\%$ constraint that is summarized in Table 3. The two line segments (i.e., tradeoff curves) are projections onto the $^{[6]}Fe^{3+}$-$^{[4]}Fe^{3+}$ plane of the $^{[6]}Fe^{3+}$-$^{[4]}Fe^{3+}$-Fe^{3+} solution domains for RT and LNT. The value of Fe^{3+}/Fe varies continuously along each segment. See text for details.

This shows that, in the present application, combining RT and LNT results leads to a unique solution. This solution is corroborated by the LHeT measurements and by an independent method that gives a measurement of Fe^{3+}/Fe from a thickness-corrected spectrum.

The thickness-corrected RT spectrum

The RT spectrum was corrected for thickness using procedures that have been described elsewhere (Rancourt, 1989; Royer, 1991). In this way, the dimensionless intrinsic absorber resonant cross section, $\sigma'_a(E)$, is obtained from the measured absorption spectrum by deconvoluting the transmission integral.

This cross section has an area of $\int dE\sigma'_a(E) = \pi/2\sigma_0\Gamma_0 n_a \bar{f}$ and is free of the artifacts from (1) thickness effects and (2) source line width. This means that the spectral features in $\sigma'_a(E)$ are much narrower than the corresponding features in the absorption spectrum, by at least Γ_0. This is seen in Figure 9, where the RT $\sigma'_a(E)$ is plotted.

Here we see that the visible Fe^{3+} contributions are much more resolved than in the raw data and that the high-energy Fe^{2+} line is much sharper. The level at 1.55 mm/s is close to the zero-resonance BG level such that the cross section can be clearly divided into two areas, irrespective of any fitting model. These are a low-energy area, A_L,

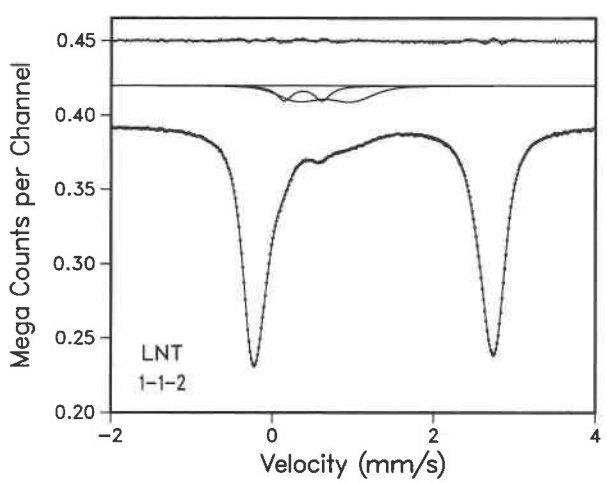

Fig. 7. The 1-1-2 fit of the LNT spectrum of our synthetic annite sample. Corresponding fit parameters are given in Table 2. The display format is the same as in Fig. 3.

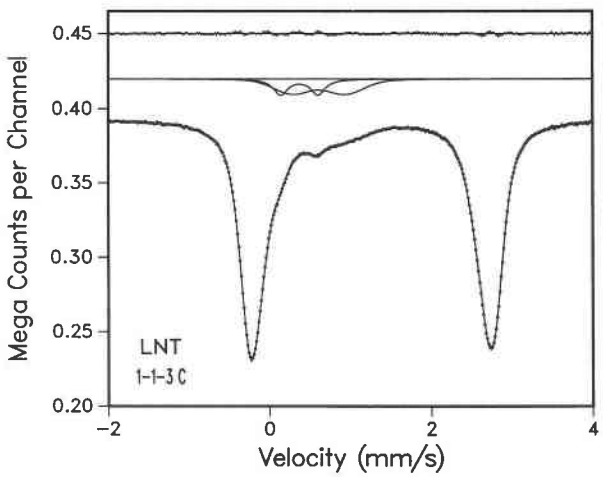

Fig. 8. Typical 1-1-3 fit (1-1-3c fit, Table 2) of the LNT spectrum. The display format is the same as in Fig. 3.

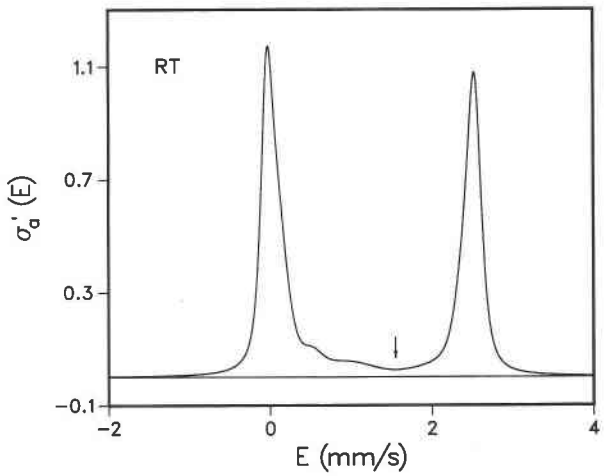

Fig. 9. RT dimensionless, intrinsic-absorber, resonant cross section $\sigma_a'(E)$ as a function of the energy E expressed in Doppler velocity units for our synthetic annite sample. The arrow at +1.55 mm/s indicates the cutoff energy used in obtaining Fe^{3+}/Fe. Note the differences between $\sigma_a'(E)$ itself and the thin-limit spectrum shown in Fig. 2. The source line width Γ_0 is convoluted into $\sigma_a'(E)$ to obtain the thin-limit spectrum.

at $E < 1.55$ mm/s and a high-energy area, A_H, at $E > 1.55$ mm/s.

Clearly then,

$$Fe^{3+}/Fe = (A_L - A_H)/(A_L + A_H) \quad (10)$$

and, since the dividing energy has a maximum uncertainty of $\sim \pm 0.07$ mm/s, we conclude that $Fe^{3+}/Fe = 11.19 \pm 0.25\%$.

This is a rigorous constraint that is devoid of any error caused by thickness effects and that does not depend on any assumed fitting model. Fitting $\sigma_a'(E)$ with a 1-1-3 model does, of course, give the same result. This constraint reduces the RT tradeoff line (Fig. 6) to only half of its original length (preserving the high-$^{[4]}Fe^{3+}$ end) and leaves the LNT tradeoff line intact.

LHeT spectra

The spectrum at $T = 4.2$ K is shown in Figure 10, and the spectrum at $T = 7.0$ K has been shown elsewhere (Christie et al., 1991). These two LHeT spectra are virtually identical and show magnetic hyperfine splitting, as expected from the high magnetic ordering temperature.

As described previously (Christie et al., 1991), a paramagnetic Fe^{2+} contribution (labeled P in Fig. 10) may persist down to these temperatures, although most of the Fe^{2+} is magnetically split and gives rise to the main absorption lines at −1.4, +1.0, and +4.6 mm/s.

The small absorption lines at the outside edges of the spectrum (at $E \lesssim -6.0$ and $E \gtrsim +7.0$ mm/s) are entirely due to the outer lines (lines 1 and 6) of Fe^{3+} sextet contributions.

By fitting just these outer Fe^{3+} lines, without requiring that the complicated middle part ($-6 \lesssim E \lesssim +7$ mm/s) of the spectrum be fitted, we can obtain populations of Fe^{3+} that contribute to these outer lines. We assume 3:2:1:1:2:3 sextet ratios and find $Fe^{3+}/Fe = 10.99 \pm 0.17$ and $11.0 \pm 0.3\%$ for the spectra at $T = 4.2$ and $T = 7.0$ K, respectively. The same results are obtained independently of line shape by simply adding channel counts in appropriate ranges. The data at $T = 4.2$ K must first be linearized, since they were collected in sine rather than constant acceleration mode.

These numbers show that all of the Fe^{3+} spectra in the sample are magnetically hyperfine at LHeT. In a preliminary study, Christie et al. (1991) concluded that this was not the case. This error occurred because, at that time, the higher temperature spectra (LNT and RT) were not fully understood and had not been completely and correctly analyzed.

In addition to Fe^{3+} components being unambiguously resolved in the LHeT spectra, we note that these resolved features show a bimodal structure suggesting two families of Fe^{3+} sextets, denoted A and B in Figure 10 and corresponding to line 1 to line 6 splittings of 14.5 and 17.5 mm/s, respectively.

It is possible to estimate populations for these A and B Fe^{3+} sites by the same methods described above. The results are given in Table 3, where the Fe^{3+}/Fe numbers are also summarized. The main source of error in all these values is area tradeoff, between Fe^{3+} and Fe^{2+} for Fe^{3+}/Fe and between $^{A}Fe^{3+}$ and $^{B}Fe^{3+}$ for the A and B populations.

The values of the $^{A}Fe^{3+}$ and $^{B}Fe^{3+}$ populations (Table 3) strongly suggest that $^{A}Fe^{3+}$ should be assigned to $^{[6]}Fe^{3+}$ and that $^{B}Fe^{3+}$ should be assigned to $^{[4]}Fe^{3+}$. We therefore conclude that, in annite, the mean saturation Fe^{3+} hyperfine fields are ~45.6 and ~55.0 T for octahedral and tetrahedral sites, respectively, and that these two sites are well resolved at LHeT because their hyperfine field distribution widths are sufficiently small.

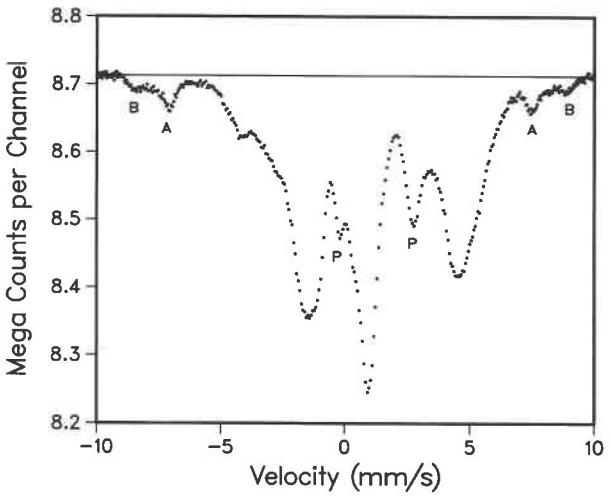

Fig. 10. The LHeT spectrum at $T = 4.2$ K of our synthetic annite sample. The flat BG level is shown by a horizontal solid line. B indicates the outer lines of the $^{[4]}Fe^{3+}$ sextet whereas A indicates the outer lines of the $^{[6]}Fe^{3+}$ sextet. P indicates the persistent paramagnetic $^{[6]}Fe^{2+}$ doublet first reported by Christie et al. (1991).

Site populations and spectral interpretation

We summarize the above results and discussion by giving final site populations: $^{[4]}Fe^{3+}/Fe = 4.00 \pm 0.15\%$, $^{[6]}Fe^{3+}/Fe = 7.00 \pm 0.20\%$, and $Fe^{3+}/Fe = 11.00 \pm 0.20\%$ (or $Fe^{2+}/Fe = 89.00 \pm 0.20\%$). These are consistent with the RT and LNT fit results illustrated in Figure 6, the Fe^{3+}/Fe number obtained from the thickness-corrected RT spectrum, and the LHeT results. They are the only numbers that simultaneously satisfy all of the model-dependent and model-independent constraints that follow from the RT, LNT, and LHeT spectra.

The final site populations for our Ni + NiO buffered synthetic annite correspond to $x = 0.210 \pm 0.006$ and $y = 0.120 \pm 0.004$ in the general structural formula for annite, assuming no octahedral vacancies:

$$K^{+}[Fe^{2+}_{3-x-y}Fe^{3+}_{x}Al^{3+}_{y}]\langle Al^{3+}_{1-y}Fe^{3+}_{y}Si^{4+}_{3}\rangle \cdot O^{2-}_{10+x+y}(OH^{-})_{2-x-y} \quad (11)$$

where square brackets represent octahedral sites and angle brackets represent tetrahedral sites. The populations imply that 16.5% of the H in the ideal structural formula is absent.

That different analysis procedures used on a given spectrum and very different spectra collected at different temperatures all lead to a unique set of site populations helps to set various aspects of the spectral interpretation.

For example, it gives us confidence in the physical correctness of the 1-1-3 fitting model used with spectra collected above T_c. This suggests that the needed defect Fe^{2+} site is indeed real and should be explained, as attempted in the next section.

Also, it helps to unravel the very complicated LHeT spectrum in that (1) this spectrum is understood not to contain a paramagnetic Fe^{3+} contribution, and (2) the magnetic hyperfine patterns of $^{[4]}Fe^{3+}$ and $^{[6]}Fe^{3+}$ are identified. That is important because the spectra collected at $T < T_c$ contain an enormous amount of information concerning both Fe^{2+} and Fe^{3+}, their local environments, and their cooperative magnetic behavior, provided the spectra can be decoded.

TABLE 3. Fe^{3+} populations from the RT thickness-corrected spectrum and LHeT spectra

T	Fe^{3+}/Fe	$A_{Fe^{3+}/Fe}$	$B_{Fe^{3+}/Fe}$
RT	11.19 ± 0.25%	—	—
7 K	11.0 ± 0.3	7.4 ± 0.4	3.6 ± 0.4
4 K	10.99 ± 0.17	7.3 ± 0.3	3.7 ± 0.3

Finally, consider the temperature dependencies of the average quadrupole splittings between LNT and RT (Tables 1 and 2). For $^{[6]}Fe^{2+}$, with a significant increase in the splitting from 2.40 to 2.88 mm/s as the temperature is lowered, the change is real and is as expected. For $^{[4]}Fe^{3+}$, having a small decrease from 0.53 to 0.47 mm/s, the splitting is essentially constant at the expected value of ~0.50 mm/s (Rancourt et al., 1992). For $^{[6]}Fe^{3+}$ (large decrease from 0.95 to 0.66 mm/s) the values are anomalous in that changes of this magnitude are not expected for Fe^{3+} ion unless substantial structural transformations occur. The anomaly is not significant, however, because the extracted Fe^{3+} quadrupole splitting values themselves are not significant. This insignificance arises from line position tradeoffs when, as is the case here, the low-energy components of relatively weak Fe^{3+} doublets are buried under the low-energy component of a strong Fe^{2+} doublet (Rancourt et al., 1992; Rancourt, 1993). Both $^{[6]}Fe^{3+}$ values (0.95 and 0.66 mm/s) are reasonable and illustrate the possible range that is consistent with the spectral data.

Defect site Fe^{2+}

In this section we propose a crystal-chemical model that explains both the measured population of the defect Fe^{2+} site ($^{*}Fe^{2+}$) and its small QS.

We note (Tables 1 and 2) that $^{*}Fe^{2+}/Fe \simeq \frac{1}{2}(Fe^{3+}/Fe) \equiv \frac{1}{2}(^{[6]}Fe^{3+} + {}^{[4]}Fe^{3+})/Fe \simeq 6\%$. If we accept the Al^{3+}/Fe^{3+} exchange idea mentioned in the introduction and Equation 11, then $^{[4]}Fe^{3+}/Fe = {}^{[6]}Al^{3+}/Fe$, and ~11% of the octahedral sites are occupied by trivalent cations that are either Fe^{3+} or Al^{3+}. The remaining ~89% of the octahedral sites are occupied by Fe^{2+}. This suggests that $^{*}Fe^{2+}$ and the trivalent octahedral cations might tend to form defect structures with 1:2 stoichiometry, with a missing H atom for each trivalent octahedral cation.

Consider the model illustrated in Figure 11, where two of 19 octahedral sites (2/19 = 10.5%) are occupied by either Fe^{3+} or Al^{3+}. Here, the 3+ ions are positioned on opposing cis sites separated by a trans site. The missing H occurs at the OH sites of the central trans site, which is the $^{*}Fe^{2+}$ site.

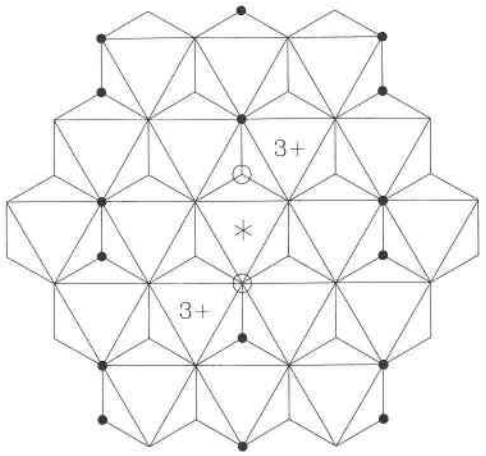

Fig. 11. Representation of the proposed octahedral layer defect structure that we associate with the $*Fe^{2+}$ defect Fe^{2+} site spectral contribution. Here, a patch of the octahedral layer is shown in which two of 19 of the octahedral sites (2/19 = 10.5%) are occupied by 3+ ions (Fe^{3+} or Al^{3+}) instead of by Fe^{2+}. The positions of the 3+ ions are indicated by 3+. Apex OH groups are represented by small solid circles. Two apex sites that, in the ideal structure, would be occupied by OH groups but that instead are occupied by O^{2-} to conserve charge balance are represented by large open circles. The location of the $*Fe^{2+}$ ion is indicated by an asterisk. The ion occupies a trans site position, whereas the 3+ ions are on opposing cis sites.

This defect structure (Fig. 11) is plausible in terms of local charge requirements and bonding rules. The central trans site may be distorted in such a way as to result in a relatively small $*Fe^{2+}$ QS.

We only propose this model as a starting point for further study. It suggests that, at low Fe^{3+} concentrations in annite, the 3+ octahedral cations prefer cis sites in opposing pairs and form cis-trans-cis complexes.

Acknowledgments

We thank G. Lamarche for performing the Squid magnetometry measurements, for helpful discussions, and for critical reading of the manuscript. We thank S. Guggenheim for critical reading of the manuscript, for helpful discussions, and for confirming our cell parameters by an independent XRD study of the same sample. We thank F.C. Hawthorne for helpful discussions. D.G.R. and A.E.L. thank the Natural Sciences and Engineering Research Council (NSERC) of Canada for financial support in the form of operating grants and I.A.D.C. and M.R. thank the NSERC for postgraduate scholarships.

References cited

Ashcroft, N.W., and Mermin, N.D. (1976) Solid state physics, 826 p. Saunders College, Philadelphia, Pennsylvania.

Christie, I.A.D., Rancourt, D.G., Lamarche, G., Royer, M., Kodama, H., and Robert, J.-L. (1991) Low temperature Mössbauer spectroscopy and magnetism of synthetic annite mica. Hyperfine Interactions, 68, 315–318.

Christie, I.A.D., Rancourt, D.G., Kodama, H., Murad, E., and Robert, J.-L. (1993) Oxidation of synthetic annite mica characterized by ^{57}Fe Mössbauer spectroscopy: Hydrogen de-intercalation and host layer valence state populations. In J.E. Fisher, P. Bernier, S. Roth, and S.A. Solin, Eds., Chemical physics of intercalation II, p. 387–391. Plenum, New York.

Dyar, M.D., and Burns, R.G. (1986) Mössbauer spectral study of ferruginous one-layer trioctahedral micas. American Mineralogist, 71, 955–965.

Eugster, H.P. (1957) Heterogeneous reactions involving oxidation and reduction at high pressures and temperatures. Journal of Chemical Physics, 26, 1760–1761.

Ferrow, E. (1987a) Mössbauer and X-ray studies on the oxidation of annite and ferriannite. Physics and Chemistry of Minerals, 14, 270–275.

——— (1987b) Mössbauer effect and X-ray diffraction studies of synthetic iron bearing trioctahedral micas. Physics and Chemistry of Minerals, 14, 276–280.

Häggström, L., Wäppling, R., and Annersten, H. (1969) Mössbauer study of iron-rich biotites. Chemical Physics Letters, 4, 107–108.

Hamilton, D.L., and Henderson, C.M.B. (1968) The preparation of silicate compositions by a gelling method. Mineralogical Magazine, 36, 832–838.

Hargraves, P., Rancourt, D.G., and Lalonde, A.E. (1990) Single-crystal Mössbauer study of phlogopite mica. Canadian Journal of Physics, 68, 128–144.

Hazen, R.M., and Burnham, C.W. (1973) The crystal structures of one-layer phlogopite and annite. American Mineralogist, 58, 889–900.

Hazen, R.M., and Wones, D.R. (1972) The effect of cation substitutions on the physical properties of trioctahedral micas. American Mineralogist, 57, 103–129.

Huebner, J.S., and Sato, M. (1970) The oxygen fugacity–temperature relationships of manganese oxide and nickel oxide buffers. American Mineralogist, 55, 943–952.

Julliot, J.-Y., Volfinger, M., and Robert, J.-L. (1987) Experimental study of carboirite and related phases in the system GeO_2-SiO_2-Al_2O_3-FeO-H_2O at P up to 2 kbar. Mineralogical Petrology, 36, 51–69.

Long, G.J., Granshaw, T.E., and Longworth, G. (1983) The ideal Mössbauer effect absorber thickness. Mössbauer Effect Reference Data Journal, 6, 42–49.

Ping, J.Y., and Rancourt, D.G. (1992) Thickness effects with intrinsically broad absorption lines. Hyperfine Interactions, 71, 1433–1436.

Ping, J.Y., Rancourt, D.G., and Stadnik, Z.M. (1991) Voigt-based methods for arbitrary-shape quadrupole splitting distributions (QSD's) applied to quasi-crystals. Hyperfine Interactions, 69, 493–496.

Rancourt, D.G. (1989) Accurate site populations from Mössbauer spectroscopy. Nuclear Instruments and Methods in Physics Research, B44, 199–210.

——— (1993) Mössbauer spectroscopy of tetrahedral Fe^{3+} in trioctahedral micas—Reply. American Mineralogist, 78, 669–671.

Rancourt, D.G., and Ping, J.Y. (1991) Voigt-based methods for arbitrary-shape static hyperfine parameter distributions in Mössbauer spectroscopy. Nuclear Instruments and Methods in Physics Research, B58, 85–97.

Rancourt, D.G., Daniels, J.M., and Lam, H.-Y. (1985) A ^{57}Fe Mössbauer study of Fe_2As: A magnetically induced electric-field-gradient asymmetry. Canadian Journal of Physics, 63, 1540–1547.

Rancourt, D.G., Dang, M.-Z., and Lalonde, A.E. (1992) Mössbauer spectroscopy of tetrahedral Fe^{3+} in trioctahedral micas. American Mineralogist, 77, 34–43.

Rancourt, D.G., McDonald, A.M., Lalonde, A.E., and Ping, Y.J. (1993) Mössbauer absorber thicknesses for accurate site populations in Fe-bearing minerals. American Mineralogist, 78, 1–7.

Royer, M. (1991) Site-specific ^{57}Fe Mössbauer recoilless fractions in true trioctahedral micas, 111 p. M.Sc. thesis, University of Ottawa, Ottawa, Canada.

Vedder, W. (1964) Correlations between infrared spectrum and chemical composition of mica. American Mineralogist, 49, 736–768.

Wones, D.R., Burns, R.G., and Carroll, B.M. (1971) Stability and properties of synthetic annite (abs.). Eos, 52, 369–370.

Manuscript received August 3, 1992
Manuscript accepted September 14, 1993